



Effect of Powder Feed Rate of Plasma-Sprayed Fe–Cr–Mo–B–C Coatings on Microstructure, Tribology and Corrosion in 3.5% NaCl Solution

Ahmad A. Sorour^{1,2} · Akeem Yusuf Adesina² · Mohamed A. Hussein² · Bander F. Al-Daajani³

Received: 29 August 2021 / Accepted: 26 February 2022 / Published online: 11 May 2022
© King Fahd University of Petroleum & Minerals 2022

Abstract

Many process parameters of air plasma spray, such as deposition power, speed, and working distance, significantly influence the resulting microstructural, mechanical, tribological, and corrosion properties of the deposited coatings. Among these parameters, the feed rate plays a vital role in the microstructural evolution and achieved properties. Thus, this study investigates the effect of feed rates (10, 20, and 45 g/min) on the microstructure, tribological, and corrosion of Fe–Cr–Mo–B–C composite coatings fabricated using air plasma spray. The results showed that as the powder feed rate was reduced, the thickness, porosity, and amorphous fraction of the coating decreased due to a higher temperature and velocity of the particles at the point of impact. The lower feed rate increased the formed crystalline phases (Fe, Cr, Mo)₂₃C₆ and (Fe, Cr, Mo)₇C₆, which were embedded in the amorphous matrix. As a result, the hardness increased from about 0.72 GPa (at 45 g/min feed rate) to about 1.0 GPa (at 20 g/min feed rate) and 1.3 GPa (at 10 g/min feed rate). Similarly, the elastic modulus increased from about 40 GPa at 45 g/min feed rate to about 52 and 68 GPa at 20 and 10 g/min feed rates, respectively. Consequently, the sliding wear resistance was improved by up to 27 and 50% at a reduced feeding rate of 20 and 10 g/min, respectively. The principal wear mechanisms were adhesion and oxidation. The electrochemical corrosion resistance in a 3.5% NaCl solution was significantly increased at the lowest feed rate.

Keywords Coating · Corrosion · Wear · Metallic matrix composites

1 Introduction

Fe-based amorphous alloy coatings have recently attracted consideration for utilizations in the military, nuclear, oil, and gas industries because of their enhanced resistance to corrosion and wear [1, 2, 3]. Many studies [3–5] explored the effect of the coating deposition techniques and the process parameters on the resulting properties. Employing the air plasma spray technique to obtain amorphous alloy coatings

is becoming attractive due to its high plasma temperature (up to 10,000 °C) and rapid cooling rate (10^5 – 10^7 K/s) [6, 7]. The corrosion and wear properties of amorphous alloy coatings depend mainly on the microstructure, composition, and amorphous phase fraction [6, 8, 9]. Thus, the corrosion resistance of Fe–Cr-based amorphous alloys/coatings has been reported to considerably exceed that of austenitic steels [10–12], Ni-based, Cu-based, Zr-based coating systems, etc. [13]. Also, these coatings have been reported to exhibit high wear resistance and excellent tribological properties [2, 3]. Based on these advantages, several investigations have been conducted to explore the properties of this coating through the variation of the composition [13, 14]. Additionally, different coating deposition techniques as well as the influence of the process parameters on the resulting properties were also being explored [3–5]. The use of the air plasma spray deposition technique to obtain amorphous Fe–Cr-based coatings is becoming suitable and attractive due to its exceedingly high plasma temperature in the range of 8000–10,000 °C and high cooling rate in the range of 10^5 – 10^7 K/s [6, 7]. This is coupled

✉ Ahmad A. Sorour
sorour@kfupm.edu.sa

¹ Department of Mechanical Engineering, King Fahd University of Petroleum & Minerals (KFUPM), Dhahran 31261, Saudi Arabia

² Interdisciplinary Research Center for Advanced Materials, King Fahd University of Petroleum & Minerals (KFUPM), Dhahran 31261, Saudi Arabia

³ Research & Development Center, Saudi Aramco, Dhahran 31311, Saudi Arabia



with the ease and flexibility of the process operation as well as being comparatively economical [15]. Studies of multi-component amorphous coatings revealed the dependence of the properties on the microstructure, composition, and amorphous phase fraction of the coating. Dense structure coupled with high glass-forming ability that is attainable with careful selection of feedstock materials, composition, and the optimization of the process parameters can greatly enhance the amorphous phase fraction and thus improved the corrosion and wear properties of the coating [6, 8].

Fe–Cr–Mo–B–C coatings have attracted significant interest due to their combination of improved corrosion resistance and enhanced mechanical properties sequel to their favorable elemental composition and microstructure. Yang et al. [16] deposited $\text{Fe}_{43}\text{Cr}_{16}\text{Mo}_{16}\text{C}_5\text{B}_{20}$ and $\text{Fe}_{43}\text{Cr}_{16}\text{Mo}_{16}\text{C}_{15}\text{B}_{10}$ coatings on mild steel using air plasma spray and obtained about 47 and 64% amorphous fraction, respectively, with relatively low porosity (below 2.5%). They found improved tribological properties with a higher amorphous fraction. The microstructure and mechanical properties of $\text{Fe}_{50}\text{Cr}_{24}\text{Mo}_{20}\text{B}_{2.6}\text{Si}_{2.4}$ coating deposited on stainless steel were investigated at different plasma currents [2]. As the plasma current increased, the porosity decreased and mechanical properties improved. The presence of Mo, B, and C in the coating further enhances both the wear and corrosion resistance [17, 18]. The integrity and reproducibility of the coatings are susceptible to the process parameters such as arc current, plasma gas composition, powder feed rate, and stand-off distance [18]. The stand-off distance, particle temperature, and velocity are known to reduce porosity and oxides content [17].

While the effect of plasma current, stand-off distance, gas composition, and particle size on the properties of Fe-based coatings have been extensively investigated [2, 6, 14, 19–23], scarce literature exists about the effect of the powder feed rate. Pukasiewicz et al. [24] studied the effect of spraying parameters on particle velocity, temperature, and residual stress formation. They found that a lower powder feed rate results in increased particle velocity and compressive residual stress. The feed rate affects the thermal input per unit mass per unit time, and thus it influences the particle temperature (and melting) and its impingement velocity [21]. The temperature and impact velocity of the particles during deposition directly affects the residual stress formation, which is related to the hardness of the coating. Despite this effect, the influence of the feed rate on the corrosion and tribological properties of $\text{Fe}_{50}\text{Cr}_{24}\text{Mo}_{20}\text{B}_{2.6}\text{Si}_{2.4}$ coatings on carbon steel has been seldomly investigated. Therefore, this study explores the impact of powder feed rate on the tribology and corrosion of Fe–Cr–Mo–B–C coatings deposited using the plasma spray process on the mild steel substrate. The surface microstructural analysis and mechanical properties were also assessed. The wear and corrosion resistance

Table 1 Plasma spray deposition parameters

Deposition parameter	Value
Deposition current	500 A
Deposition voltage	70 V
Deposition speed	4 mm/s
Working distance	102 mm
Coating passes	12 × 2
Preheat speed	5 mm/s
Preheat passes	8

were determined and correlated with the microstructure and mechanical properties.

2 Experimental Procedure

2.1 Materials and Coating Deposition

The chemical composition of the amorphous alloy powder selected for this investigation was 52–54%Fe, 25–27%Cr, 16–18%Mo, 2–2.2%B, and 2–2.5%C (all in wt.%). More details about the powder can be found in the previously published work [25]. Samples of 1018 carbon steel with a dimension of 50 × 25 × 3 mm were used as a substrate. The samples were sandblasted and cleaned with acetone before the deposition.

The amorphous alloy powder was deposited using an air plasma spray system (Oerlikon Metco, Switzerland) with the parameters listed in Table 1. The deposition was conducted in an environment consisting of Ar and H₂ with an individual gas flow rate of 78.8 and 4.7 l/min, respectively. Three coating samples were prepared using 45, 20, and 10 g/min powder feed rate and they were labeled S45, S20, and S10, respectively.

2.2 Characterizations and Mechanical Properties

Structure and microstructure characterizations of the coatings were performed using x-ray diffraction (Advance D8 XRD, Bruker, USA), a scanning electron microscope (SEM, VEGA3 SBH, TESCAN, Czech Republic), and an energy dispersion spectrometer (EDS, Oxford, USA). The XRD analysis was conducted to identify the coating structure and phases using a diffractometer employing a Cu K_{α} ($\lambda = 0.15406$ nm) radiation and under the operation condition of 40 kV and 40 mA. The samples were scanned with 0.02°/s for 1 s/step over diffraction angles range of 20–90°. The SEM analysis was performed to investigate morphology and microstructure as well as to measure the coating thickness.

The EDS analysis was carried out to identify composition qualitatively.

The roughness of the coating surface was measured using an optical profilometer (Contour GT-K, Bruker, Germany). A total area of 18.26 mm² from five different 1.66 × 2.2 mm spots on the coated samples was captured with a pixel resolution of 1632 × 786. The average arithmetic mean (Ra) was estimated from the captured 3D images.

The porosity of the coatings was estimated from the cross-sectional SEM images. A minimum of three images at a magnification of 3000 × with an image size of approximately 46 × 46 μm² per coating was analyzed using Fiji (ImageJ and variants) software [26]. After the calibration of the image, it was then converted to an 8-bit image. The threshold method was used to exclude the gray areas, while the circularity and porosity size were set from 0.5 to 1 and zero to infinity, respectively.

The microhardness and elastic modulus were measured using a micro indenter (MicroCombi tester CSM Instruments, USA), and calculated based on the Oliver and Pharr method [27]. A maximum load of 0.1 N was applied for a dwelling time of 10 s and a loading/unloading time of 150 s. This applied load resulted in a maximum penetration depth of less than 10% of the coating thickness. An average of five indentations is reported.

2.3 Tribology and Corrosion Tests

The coefficient of friction and wear resistance of the coatings were investigated using a ball-on-flat linear reciprocating tribometer (TR-282, Ducom Instruments, India). The tests were conducted in the dry sliding condition in the air at ambient temperature (23 ± 5 °C) and room humidity (50 ± 5%RH). The counterpart was an alumina ball with a 6 mm diameter. A load of 5 N was applied for a total reciprocating distance of 250 m, a track length of 5 mm, and a sliding speed of 100 mm/s. The mass loss of the worn samples and counterpart balls was measured using a weight balance (AB-224, Phoenix Instrument, Germany) with a readability of 0.1 mg and reproducibility of less than 0.2 mg. The wear rate was calculated and expressed as mass loss per total sliding distance per applied load (mg/N.m). The SEM and EDS analyses of the worn surfaces were attained to study the wear mechanisms.

The electrochemical corrosion resistance and behavior of the coatings were assessed in a 3.5% NaCl solution. The corrosion tests were executed using a potentiostat (Reference 3000, Gamry Instruments, USA) with a three-electrode cell set-up: a saturated calomel electrode (SCE) as the reference electrode, the coated sample as the working electrode, and graphite rod as the counter electrode. For the electrolytic system to attain an equilibrium state, the open-circuit potential (OCP) was maintained for 1 h. Linear polarization resistance

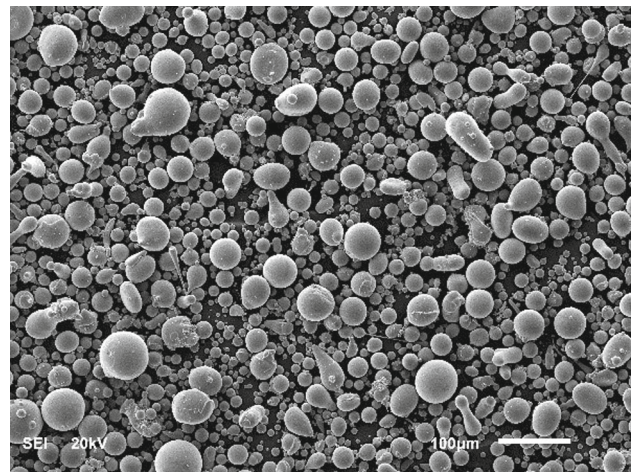


Fig. 1 SEM micrograph of the starting Fe–Cr–Mo–B–C powder

(LPR) was then performed with a scan rate of 0.125 mV/s and between -20 and + 20 mV against OCP. Subsequently, the potentiodynamic polarization (PDP) test was conducted with a scan rate of 0.179 mV/s polarized by ± 0.5 V away from the OCP. The corrosion potential E_{corr} and current density i_{corr} were obtained from the Tafel extrapolation of the anodic and cathodic curves. An exposed sample area of 0.56 cm² was used for all corrosion tests.

3 Results and Discussion

3.1 Microstructure Characterizations

Figure 1 shows the morphology of the starting Fe–Cr–Mo–B–C powder. The powder particles are typically spherical and have a size of 31 ± 10 μm in diameter, as measured in an earlier study [25]. The powder was deposited using an air plasma spray system to fabricate three coating samples using 45, 20, and 10 g/min powder feed rates (labeled S45, S20, and S10, respectively). Figure 2 demonstrates the cross-section SEM micrographs of these coated samples. As the powder feed rate was reduced from 45 g/min (S45) to 20 g/min (S20) and 10 g/min (S10), the thickness decreased drastically. Since the deposition duration and other deposition parameters were kept constant for the three coatings, this thickness variation is expected because the total volume of powders deposited dramatically differs.

Figure 3 shows higher magnification SEM micrographs of the cross section and surface of the coating. The cross-sectional images (Fig. 3 (a, c, and e)) show typical defects of plasma spray coatings, including un-melted particles, partially melted particles, pores, and oxides which were confirmed by EDS analysis. Similar defects can also be noticed on the surface morphological images (Fig. 3b, d, and f). The

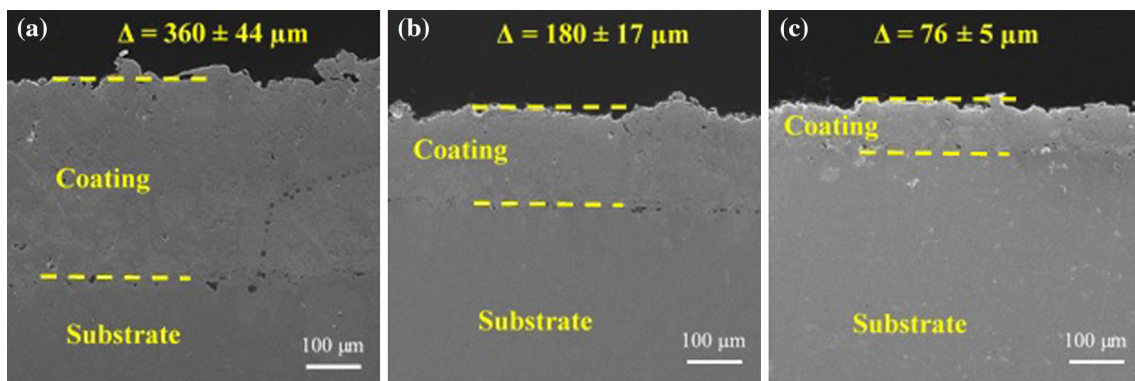


Fig. 2 SEM cross-section micrographs of the coated samples **a** S45, **b** S20, and **c** S10 deposited using different powder feed rates

coating deposited with the higher feed rate (sample S45) possessed a more significant number of unmelted and partially melted particles (splats) than the coatings deposited with lower feed rates (S20 and S10). The percentage of fully melted particles increased as the feed rate reduced to 10 g/min (S10), which can be associated with the thermal input per unit mass of powder per unit time. When the powder feed rate increases, the thermal input per unit mass per unit time is reduced, and consequently, the particle temperature and velocity at the point of impacting the substrate decrease [18]. Previous studies [28, 29] found that by increasing the feed rate of alumina powders from 10 to 20 g/min, the particle velocity was reduced from 255 to 247 m/s. As a result, some powder particles reached the substrate without being melted due to the lower thermal energy of the particle. It is evident from the microstructure of sample S10 (Fig. 3(e, f)) that fewer partially melted particles can be observed. Similarly, more splats (fully melted particles) could be seen in sample S10 compared to sample S20 (Fig. 3(c, d)), which is characterized by more partially melted particles. The protrusion of partially melted particles in S20 is an indication of the reduced thermal energy. Figure 3a, b shows that sample S45 demonstrates a higher proportion of unmelted and partially melted particles.

Figure 4 demonstrates the 3D optical profilometer images of the coatings. The surface topography of S45 (Fig. 4a) exhibited a higher degree of irregularity and many peaks and valleys compared to sample S20 (Fig. 4b). The sample S10 (Fig. 4c) demonstrated the smoothest surface topography. The surface roughness (arithmetic mean parameter, R_a) measured from the 3D optical profilometer is represented in Table 2. The surface roughness of the coatings indicates that as the powder feed rate decreased from S45 to S10, the roughness decreased. The coated sample S10 exhibited the lowest R_a values, while S45 and S20 had a similar roughness. Molten particles (splats) can easily conform with the previous splats, unlike unmolten or partly molten particles. On the other hand, the unmelted or partially melted particles (Figs. 3b and d)

result in higher surface roughness. The R_a value decreases as the feed rate decreases because of the increasing velocity and temperature. This increase (in the velocity and temperature) is due to the reduction in the momentum of the particle at impact and the higher heat input per unit mass per unit time. A similar observation has been reported by Pawlowski [28]. The flattening ratio governed by the kinetic energy spreading might be higher at a higher feed rate, contributing to higher roughness [30].

The porosity of the coatings is presented in Table 2. The coating S45 has the highest porosity (1.4%), while the coating S10 deposited with the lowest feed rate possessed the lowest porosity (0.9%). The S20 coatings showed a porosity of 1.1%. Therefore, the estimated porosity in the coatings showed a direct implication of the efficiency of the deposition process. High porosity resulted from the higher powder feed rate because of the low thermal energy input per particle, which leads to an increased number of unmolten particles. This is associated with the fact that unmolten particles cannot conform properly upon impact on previously existing splats/particles, resulting in more voids and porosities. Similar results reported by Zhou et al. [31] indicate that the porosity of $\text{Fe}_{48}\text{Cr}_{15}\text{Mo}_{14}\text{C}_{15}\text{B}_6\text{Y}_2$ reduced with the decrease in the deposition rate due to the consequent higher temperature of particles and thus, they are accelerated to higher velocities.

Figure 5 shows the XRD spectra of the starting powder and deposited coatings. The XRD spectrum of the powder has a broad diffuse peak (at $2\theta = \sim 44^\circ$), which is a typical amorphous peak of FeCrMo-based amorphous material. The XRD spectra of the coated samples exhibit that partially amorphous/nanocrystalline composite coatings have been obtained. The crystallite size was estimated using Scherrer's equation based on the observed crystalline peaks at a diffraction angle of 38.3° for samples S20 and S10 with profound crystalline phases. The crystallite size was estimated to be approximately 10 and 9 nm for samples S20 and S10, respectively. Because Scherrer's equation does not

Fig. 3 SEM micrographs of the cross section (**a, c, e**) and surface morphology (**b, d, f**) of sample; **a, b** S45, **c, d** S20, and **e, f** S10

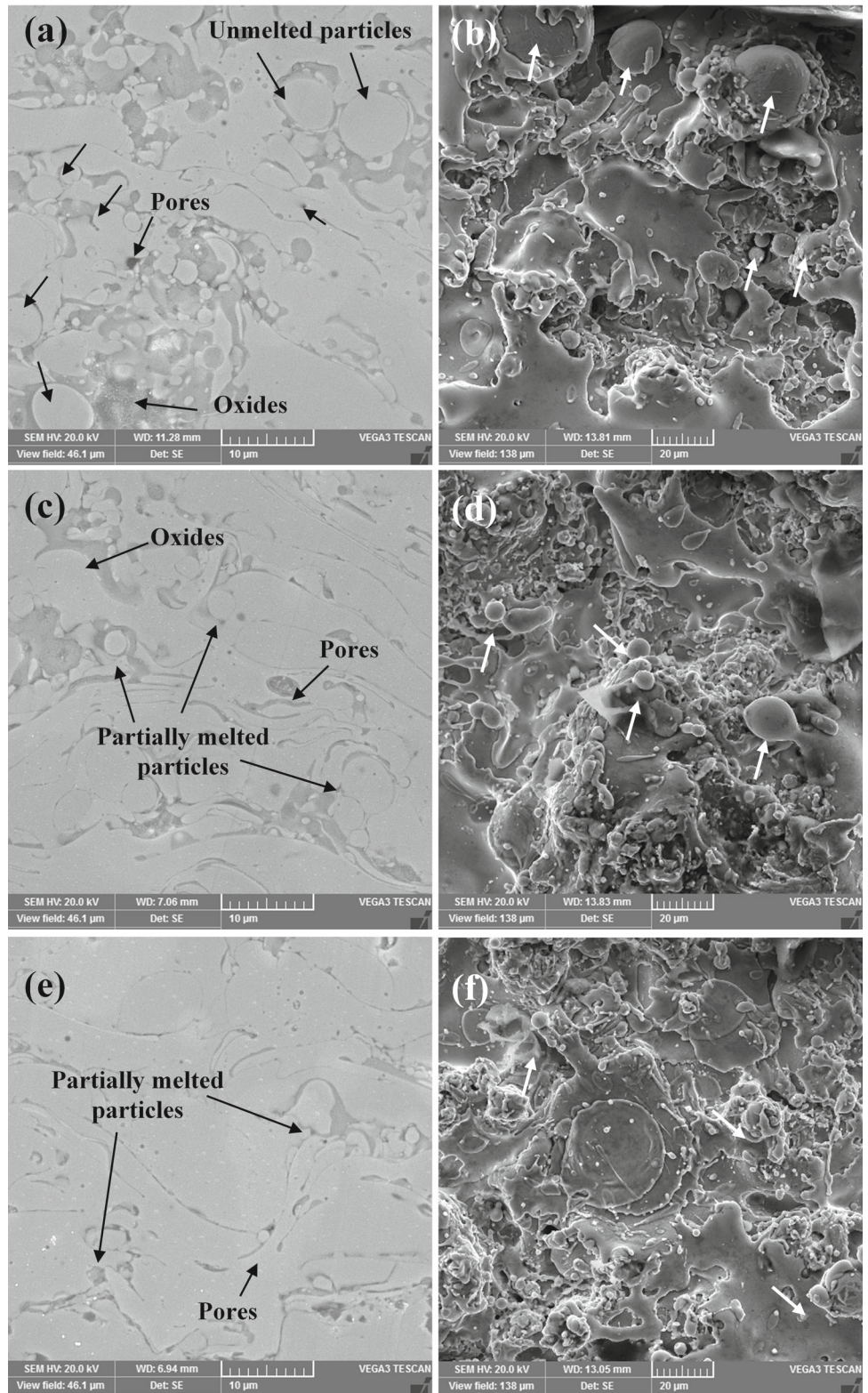


Fig. 4 The 3D surface profilometry images showing the topography of **a** S45, **b** S20, and **c** S10 coatings

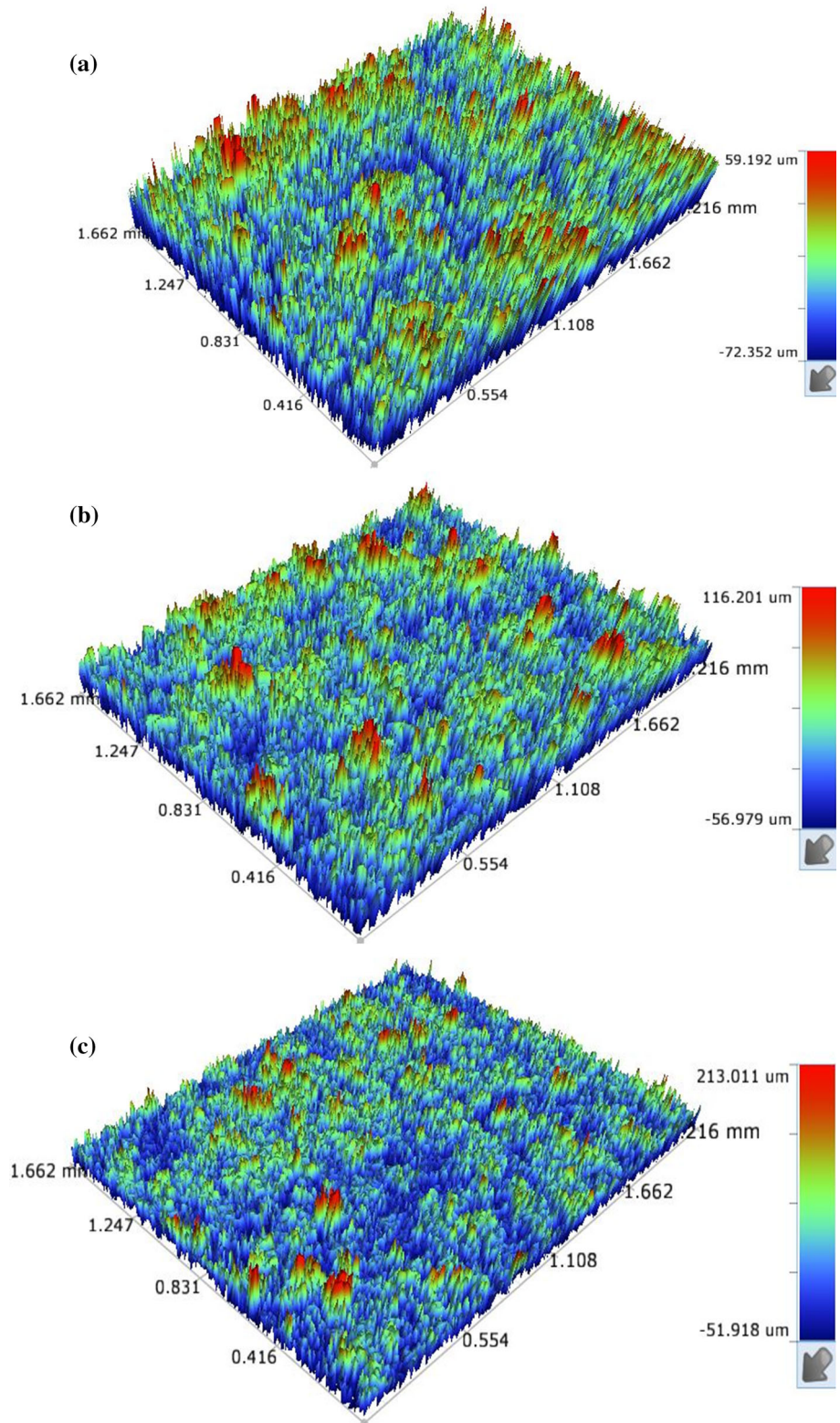
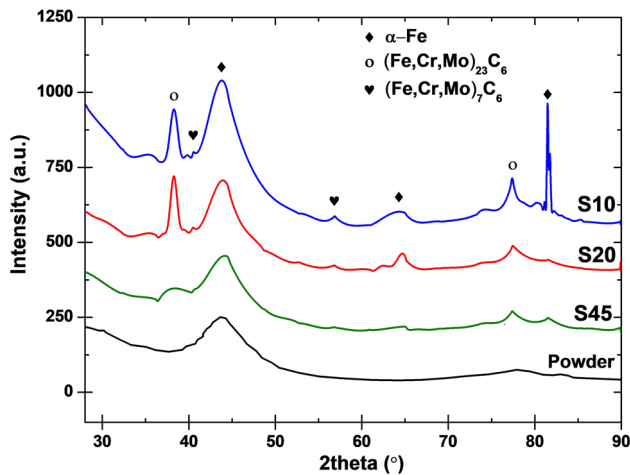


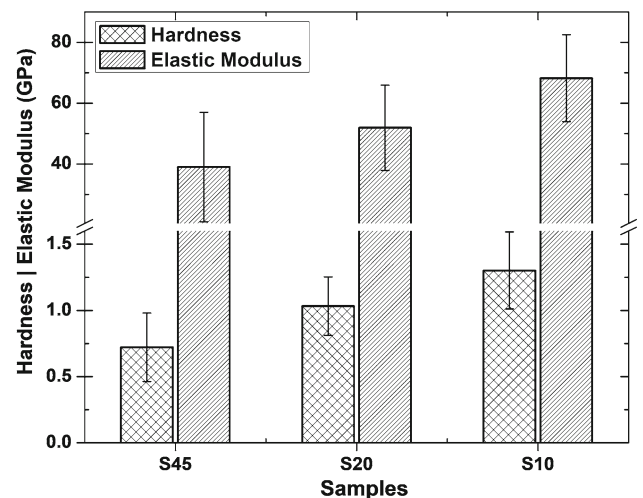
Table 2 The estimated surface roughness, porosity, and a fraction of amorphous and crystalline phases in the starting powder and deposited coatings

Samples	R _a (μm)	Porosity (%)	Amorphous Phase (%)	Crystalline phase (%)
Powder	–	–	100	–
S45	11.22 ± 1.7	1.42 ± 0.13	89.06	10.94
S20	11.01 ± 0.8	1.05 ± 0.04	64.16	35.84
S10	9.62 ± 0.9	0.92 ± 0.05	56.24	43.76

**Fig. 5** XRD results of the starting powder and deposited coatings

account for micro-strain and peak broadening resulting from the instrument, these crystallite size values should be considered the least sizes.

The observation of the new peaks and their estimated crystallite sizes substantiates the formation of new phases that are nanocrystalline. Coating S45 is almost completely amorphous but had very few formed crystalline phases, but the crystalline size of S45 was not estimated due to the possibility of being overlapped or confused with the amorphous peaks. With a decrease in the feed rate for coating S20, sharp peaks were observed. More crystalline peaks were noticed with further reduction in the feed rate (sample S10). However, the amorphous peak at $2\theta = \sim 44^\circ$ was almost indiscernible. The results indicate that as the feed rate decreased, the deposition velocity and temperature at impact increased, and thus more partial devitrification occurs. In other words, higher deposition velocity increases the kinetic energy of the particles at impact and thus results in an increase in the localized temperature at impact to values that favor the process of devitrification/crystallization. During the primary devitrification process, the primary crystalline phases form in a matrix of the remaining amorphous phase through a diffusion-controlled growth mechanism [32, 33]. These crystalline phases correspond to $(\text{Fe, Cr, Mo})_{23}\text{C}_6$ and $(\text{Fe, Cr, Mo})_7\text{C}_6$, and similar phases have also been reported by several researchers [25, 34–36]. Using the method described in the references [37] [38], the fractions of amorphous and crystalline phases were

**Fig. 6** Hardness and elastic modulus of the coatings

estimated and are presented in Table 2. The coating S45 has a low crystalline phase fraction ($\sim 11\%$). As the powder feed rate decreased, the fraction of the crystalline phase increased dramatically to about 36% for S20 and about 44% for S10. Thus, to maintain the amorphous phase of the starting powder, the feed rate should be as high as possible.

3.2 Hardness and Elastic Modulus

The hardness and elastic modulus of the coatings were measured using microindentation, and the results are shown in Fig. 6. As the powder feed rate was reduced, the hardness and modulus of elasticity increased. The hardness and elastic modulus of sample S45 were 0.72 ± 0.16 GPa and 40 ± 8 GPa, respectively. Similarly, the hardness was increased for samples S20 and S10 to 1.0 ± 0.12 and 1.3 ± 0.19 GPa, respectively. Furthermore, the elastic modulus also increased to 52 ± 4 and 68 ± 4 GPa for samples S20 and S10, respectively. Thus, by reducing the feed rate from 45 g/min (S45) to 20 g/min (S20), about a 45% increment in the hardness was obtained, while 80% hardness improvement was achieved with a further reduction to 10 g/min (S10). A similar trend was observed for the elastic modulus. The hardness of Fe-based coatings is usually influenced by several parameters such as feedstocks and other deposition parameters. These

parameters affect the coating's degree of compactness, porosity, microstructure, crystallinity, phases, and defects that determine the coating hardness and other mechanical properties [2, 28, 39]. The cooling rate as well may cause thermal residual stresses within the coating that increase the coating hardness [40]. Nevertheless, the unmelted particles might act as a second phase reinforcement, which may increase the hardness and elastic modulus [41].

In the deposited coatings, the hardness was mainly determined by the amount of the crystalline reinforcement phases and the porosity of the coatings (Table 2). As the porosity decreased, the density of the deposits increased, and thus, the hardness increased, as shown in Table 2. The sample S45 with the highest porosity and lowest crystallinity demonstrated the lowest hardness and elastic modulus, while the sample S10 with the lowest porosity and highest crystallinity exhibited the highest hardness and elastic modulus. When the reinforcement crystalline phases fraction increased, hardness increased as a result of the crystalline phases induced more restriction to dislocation movement and plastic deformation. Similarly, it has been reported that the hardness of the amorphous coating is enhanced by increasing the percentage of the reinforcement phases [39]. Additionally, as the thickness increases, there is the likelihood of increased porosity due to the peening effect of the incoming particle [31]. This increase in porosity may be associated with the causes for the reduction in the mechanical properties of the S45 sample with the highest feed rate.

3.3 Friction and Wear Resistance

Dry sliding wear test of the coatings deposited by plasma spray onto 1018 carbon steel was conducted against alumina ball counterface for 250 m sliding distance. Figure 7a shows the COF as a function of sliding distance for S45, S20, and S10 coatings. The average steady-state COF of the samples is 1.2 ± 0.1 , 1.0 ± 0.1 , and 0.9 ± 0.1 for S45, S20, and S10, respectively. A similar COF value has been reported for Fe-based coating deposited by HVOF [5, 42]. After 100 m sliding distance, S20 and S10 exhibited equivalent steady-state COF. However, S45 showed a higher and unstable COF, most probably due to the higher porosity and surface roughness [43]. Nevertheless, the COFs of the samples seem to converge after a long reciprocating distance (200 m).

The wear rates of the coated samples and the counterfaces are presented in Fig. 7b. These wear rate values are comparable to the wear rate of 48Fe-14Mo-15Cr-2Y-15C-6B (at.%) [44] and lower than that of 50Fe-18Cr-1.9Mn-7.4Mo-1.6 W-15B-3.8C-2.4Si (at.%) [45] coatings. Sample S45 demonstrated the lowest resistance to wear with a wear rate of $9 \pm 1.4 \times 10^{-4}$ mg/Nm because of the lower hardness and higher porosity compared to the other coatings. Reduction in the feed rate as in samples S20 and S10 improves the wear

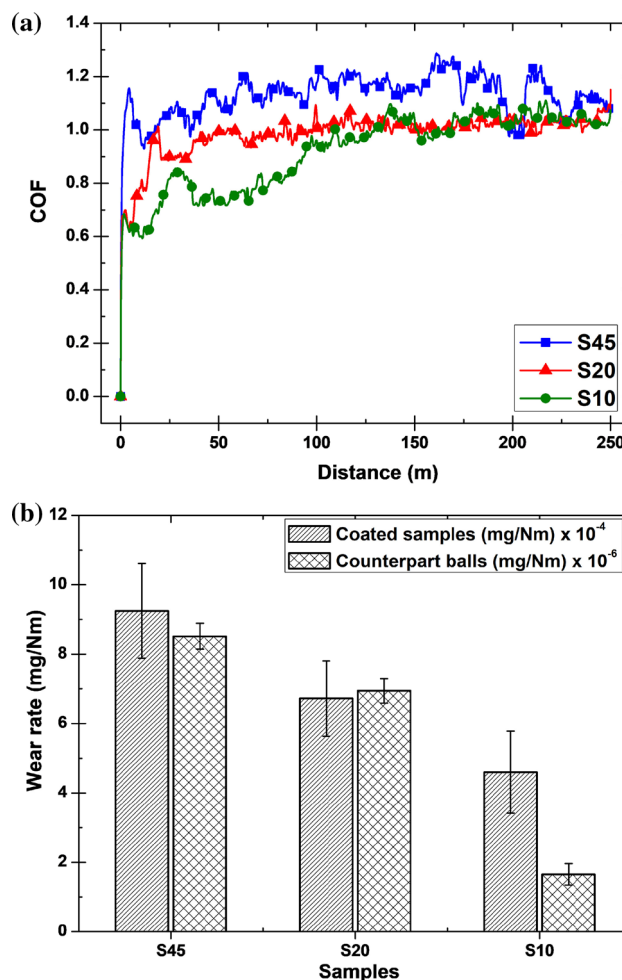


Fig. 7 a COF vs. sliding distance for the coatings, and b wear rates of the coated samples and the counterface ball

resistance by 27 and 32%, respectively. This improvement is attributed to the lower porosity and oxides, and the higher hardness.

The wear rates of the counterface exhibited a similar trend as the coatings. The counterface slid against sample S45 experienced the highest wear rate of $8.5 \pm 0.4 \times 10^{-6}$ mg/Nm, and the wear rate was reduced for samples S20 and S10 to $6.9 \pm 0.4 \times 10^{-6}$ and $1.7 \pm 0.3 \times 10^{-6}$ mg/Nm, corresponding to about 20 and 80% wear rate reduction, respectively. This similarity would be attributed due to the lowering of COF. By considering the wear rate of the system (coating and counterface), it is clear that the wear rate of the system decreased significantly as the powder feed rate decreased.

The sliding wear mechanism of the coatings was studied by post microstructural analysis of wear tracks using SEM, as shown in Fig. 8a–c. The worn surface damages encompass material removal, oxidation, and fracturing. The Fe-based amorphous matrix contained Cr and Mo oxidizes as a result of the elevated temperatures at asperities (flash temperature).

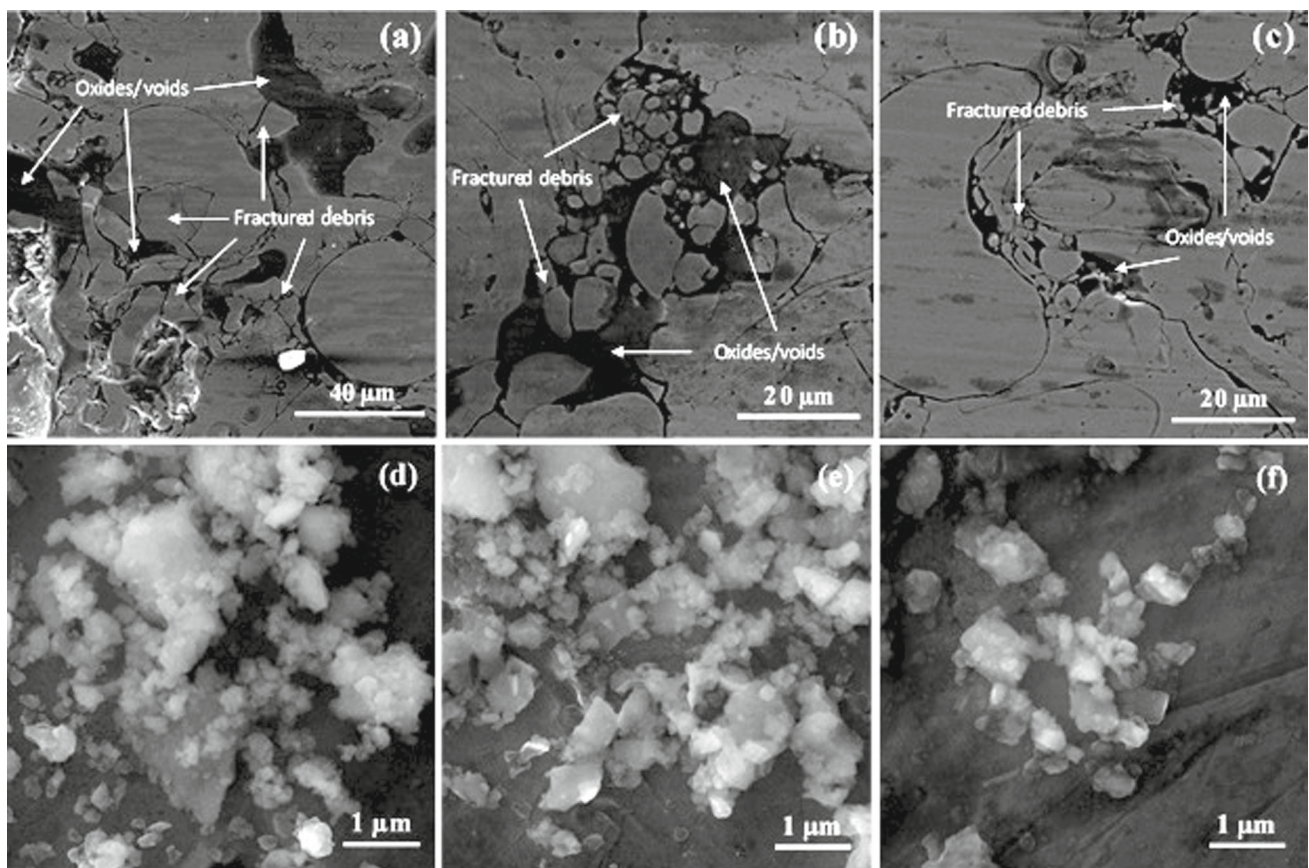
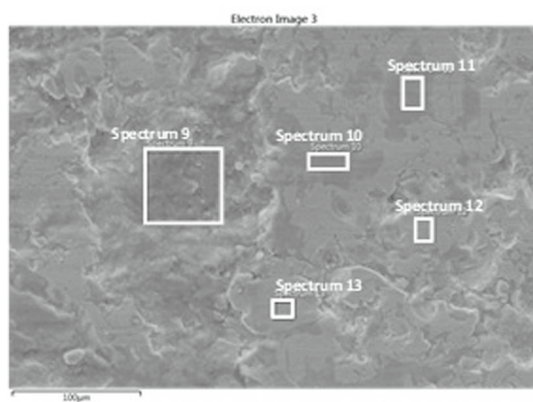


Fig. 8 Typical SEM micrographs of the wear track of samples **a** S45, **b** S20, **c** S10. Morphology of the wear debris taken from the wear track for samples **d** S45, **e** S20, and **f** S10



Composition (at.%)	Spectra				
	9	10	11	12	13
O	65.3	62.7	68.6	15.8	40.3
Fe	19.7	18.6	17.8	48.4	34.1
Cr	9.7	9.1	9.0	23.7	17.0
Mo	4.7	4.1	4.1	10.6	7.1
Si	0.6	1.0	0.6	1.5	1.4

Fig. 9 Typical EDS analysis of the wear track of the sample S20 showing the formation of oxides

This temperature might exceed 1000 °C contingent upon the applied load, sliding speed, and generated COF [46]. According to the EDS analysis (Fig. 9) of the wear track, oxide of Fe, Cr, and Mo were possibly formed, especially Fe oxides, due to the high content of Fe. These oxides formed and then were removed by the adhesion and friction forces [46, 47], forming wear debris (Fig. 8d–f). Similar debris was reported in a previous study [48]. Therefore, the main wear mechanisms were

adhesive wear and tribo-oxidation, which occurred simultaneously.

The wear scars of the alumina ball counterface slid against the coatings (Fig. 10) show grooves aligned with the sliding direction. These grooves formed because of the presence of the oxide debris that slid over the surface and scratched it. The size of the wear scars of the ball correlates with the counterface wear rate.

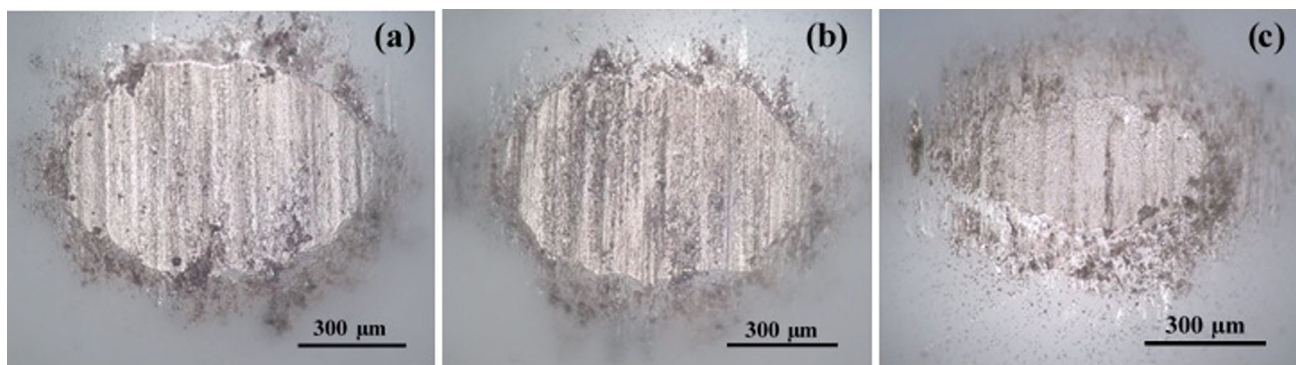


Fig. 10 Optical micrographs of the wear scar on the alumina ball counterface slid against samples **a** S45, **b** S20, and **c** S10

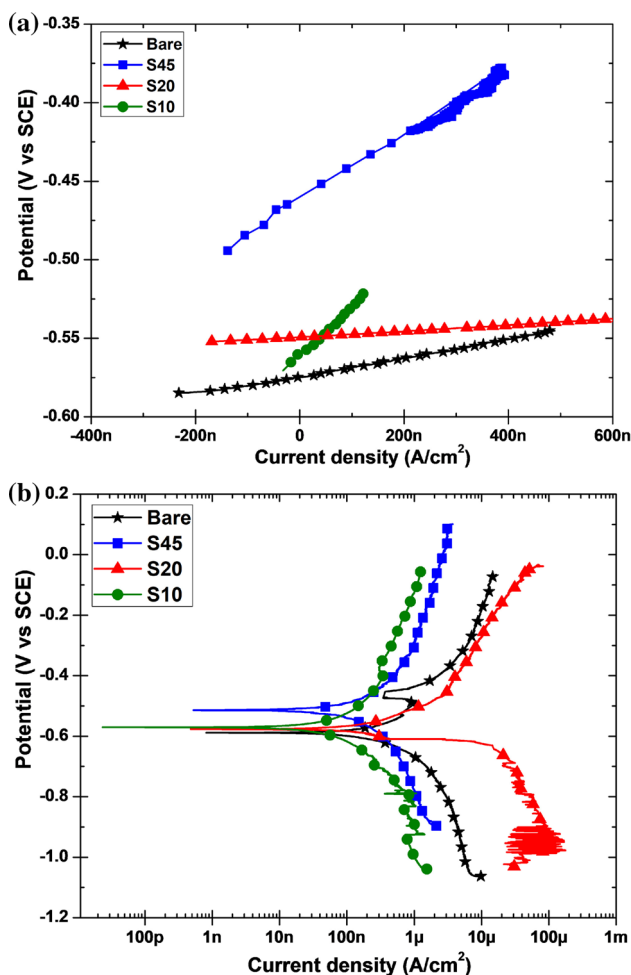


Fig. 11 **a** The LPR curves and **b** PDP curves of the tested bare and coated samples exposed to a 3.5% NaCl solution at room temperature

3.4 Corrosion Behavior

The corrosion rate of the coatings and the uncoated (bare) sample (mild steel) was measured using LPR. The LPR curves are shown in Fig. 11a, and the values of the corrosion

Table 3 Parameters obtained from the linear polarization resistance (LPR) measurement

LPR	R_p ($k\Omega\text{ cm}^2$)	I_{corr} ($\mu\text{A/cm}^2$)	E_{corr} (mV)
Bare	59.28	0.44	− 574.8
S45	229.3	0.11	− 418.0
S20	20.78	1.25	− 549.1
S10	317.6	0.08	− 559.6

parameters derived from the LPR experiment are presented in Table 3. The R_p value of the bare was about $60\text{ k}\Omega\text{ cm}^2$, while the R_p of the coated samples S45, which was deposited with a higher feed rate of 45 g/min , is four times higher. Upon increasing the feed rate to 20 g/min , as in sample S20, the R_p drastically drops below that of the substrate. However, at a low feed rate (sample S10), the R_p value increased to almost $320\text{ k}\Omega\text{ cm}^2$ demonstrating the highest resistance and the best protective performance.

The PDP test was also conducted to provide better insight into the corrosion behavior of the coatings, and the PDP curves for the bare and coated samples are shown in Fig. 11b. The extracted data; the corrosion potential (E_{corr}), corrosion current density (i_{corr}), and corrosion rate (in mpy), from the PDP curves using the Tafel slope [49], are shown in Table 4. The E_{corr} of the coated samples is shifted to the higher potentials in comparison with that of the bare, indicating their lower susceptibility to corrosion, except for sample S20. Furthermore, the i_{corr} and the corrosion rate were also observed to be lower in comparison with the bare. Sample S10 possessed the lowest i_{corr} , while sample S20 demonstrated the worst corrosion resistance due to it exhibiting the highest i_{corr} among the coatings and the bare. This behavior is in agreement with the trend observed from the LPR results (Table 3). The enhanced performance of sample S10 may be attributed to the effective deposition parameter, which enables the deposition of coating with lesser pores, high crystallinity, which enhances the formation of the protective oxide layer, and the

Table 4 Parameters obtained from Tafel fitting of the potentiodynamic polarization (PDP) measurement

PDP	β_a (mV/dec.)	β_c (mV/dec.)	I_{corr} ($\mu A/cm^2$)	E_{corr} (mV)	CR (mpy)
Bare	218	232	0.55	− 589	0.45
S45	266	321	0.26	− 514	0.20
S20	106	173	13.1	− 594	10.7
S10	330	360	0.16	− 571	0.13

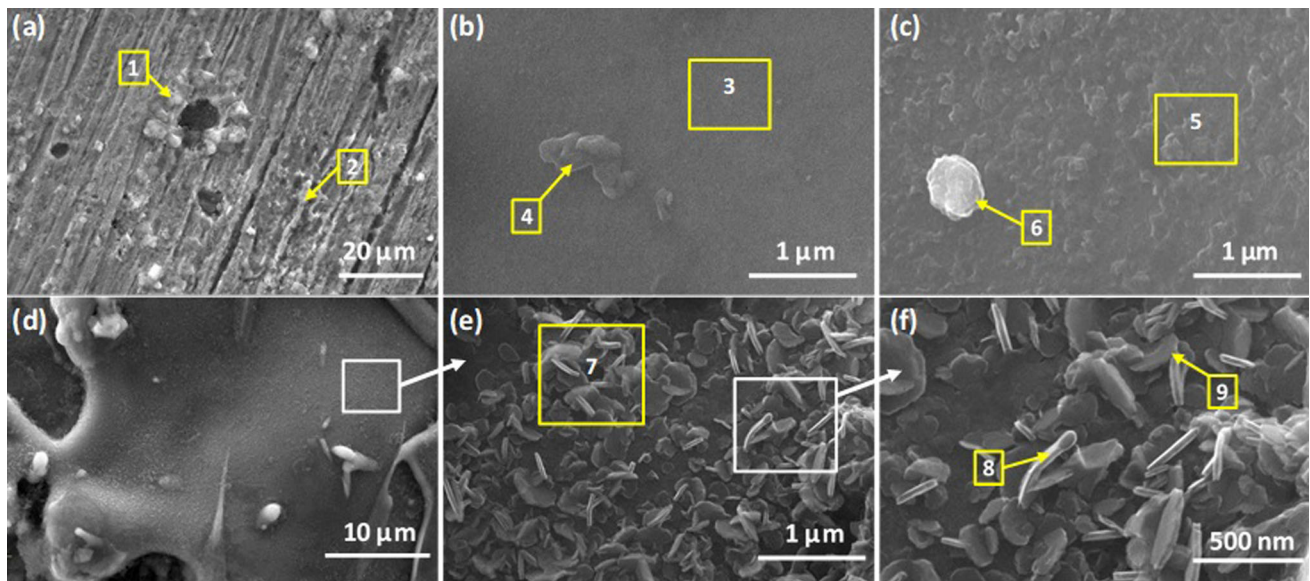


Fig. 12 SEM micrographs of the corroded samples in 3.5% NaCl. **a** bare, **b** S45, **c** S20 and **d–f** S10

Table 5 EDS analysis (in wt.%) corresponds to the notions of the corroded surfaces in Fig. 12

Notation	Fe	Cr	O	C	Mo	B/Si	Na	Cl
1	76.5	–	13.1	9.4	–	–	–	1
2	62.3	–	18.1	18.7	–	–	–	0.9
3	35.8	8.9	23.4	21	5.6	–	2.4	2.9
4	48.9	9.9	22.3	9.8	7.8	–	0.8	0.5
5	38.6	17.5	11.1	20	12.2	–	–	0.5
6	10.7	1.5	3.6	1.9	1.8	–	42.9	37.3
7	39.4	0.6	35.3	17.9	0.8	–	0.6	5.3
8	55.2	24.6	10.1	–	10.1	–	–	–
9	56.2	25.5	10.4	–	7.9	–	–	–
10	44.4	20.6	6.7	12	14.5	1.8	–	–

Notation #10 is the typical composition of the uncorroded as-deposited coating

low roughness of the coating. The result suggests that the corrosion resistance may not correlate directly with porosity but rather associated with the percentage of interconnecting pores, microstructural variation as a result of the chemistry of molten splats and unmolten/partially molten particles. Sá Brito et al. [50] reported a similar finding where the chemical composition might play a more significant role than porosity in the corrosion resistance of metallic coatings.

To investigate the corrosion mechanism, SEM and EDS analyses of the corroded surfaces of coatings and bare in 3.5% NaCl were carried out, and the results are shown in Fig. 12 and Table 5. The corroded surface of the bare sample (Fig. 12a) demonstrates pits of various sizes that formed because of the chloride attack (Table 5, Notation #1 and #2). However, no pits were noticed in the corroded surface of the coatings S45, S20, and S10 (Fig. 12b–f). The absence

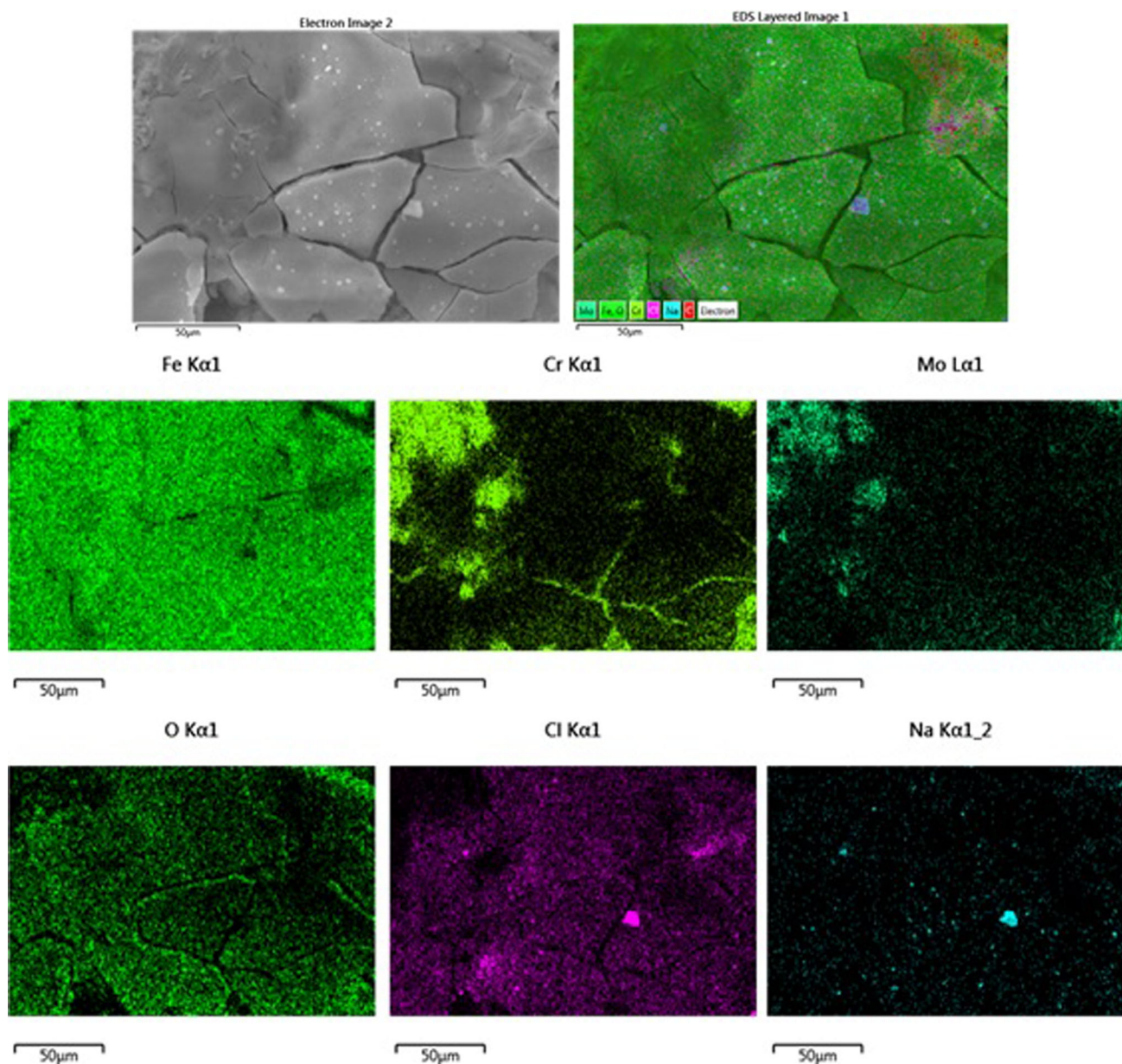


Fig. 13 EDS mapping of the corroded surface of sample S20 showing the depletion of Cr and formation of cracks under chloride attack

of pits is due to the protective capability of the coated samples against pitting. Generally, the oxygen contents increased on the surface of corroded samples (Table 5), and thus it indicates that oxide formation is the primarily effective mechanism against corrosion. Lower and higher magnifications SEM micrographs of the corroded surface of the sample S10 (Fig. 12d–f) revealed a flake-like oxide layer. These oxides are rich in both iron and chromium (#8 and #9 in Fig. 12f and Table 5). These oxides are possibly spinel of mixed iron and chromium oxides. The increase in chromium concentration in the oxides film can significantly improve the corrosion protection in the coated sample [34]. In contrast, no such similar structure was observed in the corroded area of samples S45

and S20 despite the observed increase in the oxygen concentration for both samples. Localized cracks were observed in sample S20. EDS mapping of the crack (Fig. 13) shows a significant amount of sodium and chloride from the NaCl solution and a reduction in Cr and Mo content. The cracks and the reduced Cr content can significantly weaken the protective or barrier characteristic of the coating and hence, facilitate localized corrosion attacks. This is suspected to be the main cause of the reduced corrosion resistance of sample S20.

4 Conclusion

In the present study, Fe–Cr–Mo–B–C composite coatings were fabricated using the air plasma spray process on mild steel with different powder feed rates (10, 20, and 45 g/min). The microstructure, tribology, and corrosion were investigated, and the following conclusions can be drawn.

1. The powder feed rate affected the deposition efficiency and coating properties. Decreasing the feed rate increased the crystalline-to-amorphous phase ratio and reduced the thickness, porosity, and defects of the coatings because of the higher thermal efficiency, temperature, and velocity at the impact.
2. The lower porosity and higher hard particle fraction resulted in an increase in the hardness and elastic modulus. Thus, the hardness of the samples deposited at feed rates of 45, 20, and 10 g/min was 0.75, 1.03, and 1.30 GPa, respectively.
3. The sample deposited at 45 g/min possessed the highest wear rate of $9 \pm 1.4 \times 10^{-4}$ mg/Nm because of the low hardness and high porosity of the coating. The wear rate was reduced by more than 25 and 30% after decreasing the feed rate from 45 to 20 and 10 g/min, respectively. The principal sliding wear mechanisms were observed to be adhesion and oxidation.
4. The corrosion resistance in 3.5% NaCl is enhanced with the lower feed rate, and this is most probably due to the formation of flake-like oxides rich in chromium.

It is recommended to conduct more studies of the effects of other process parameters (deposition power, speed, and working distance) on the microstructure, mechanical, tribological, and corrosion properties as well as to identify the optimized parameters for the investigated Fe–Cr–Mo–B–C composite coatings for a specific application.

Acknowledgements The authors would like to acknowledge Saudi Aramco, Saudi Arabia, for the fabrication of the coatings using plasma spray. Thanks are also expressed to King Fahd University of Petroleum and Minerals (KFUPM), Saudi Arabia for the support provided.

Funding The research was supported by Saudi Aramco, Saudi Arabia and King Fahd University of Petroleum and Minerals (KFUPM), Saudi Arabia.

Availability of data and material Available upon request.

Code availability Not applicable.

Declarations

Conflict of interest Not applicable.

Ethics approval Not applicable.

Consent to participate Not applicable.

Consent for publication Not applicable.

References

1. Suryanarayana, C.; Inoue, A.: Iron-based bulk metallic glasses. *Int. Mater. Rev.* **58**, 131–166 (2013). <https://doi.org/10.1179/1743280412Y.0000000007>
2. Kobayashi, A.; Yano, S.; Kimura, H.; Inoue, A.: Mechanical property of Fe-base metallic glass coating formed by gas tunnel type plasma spraying. *Surf. Coat. Technol.* **202**, 2513–2518 (2008). <https://doi.org/10.1016/j.surfcoat.2007.09.011>
3. Zhang, C.; Liu, L.; Chan, K.C.; Chen, Q.; Tang, C.Y.: Wear behavior of HVOF-sprayed Fe-based amorphous coatings. *Intermetallics* **29**, 80–85 (2012). <https://doi.org/10.1016/j.intermet.2012.05.004>
4. Ciswandi, Aryanto, D., Irmaniar, Tjahjono, A., Sudiro, T.: The effect of annealing on structure and hardness of (Fe–Cr)–50 at.% Al coatings synthesized by mechanical alloying. AIP Conference Proceedings. 1964, (2018). Doi:<https://doi.org/10.1063/1.5038287>
5. Ma, H.R.; Li, J.W.; Jiao, J.; Chang, C.T.; Wang, G.; Shen, J.; Wang, X.M.; Li, R.W.: Wear resistance of Fe-based amorphous coatings prepared by AC-HVAF and HVOF. *Mater. Sci. Technol.* **33**, 65–71 (2017). <https://doi.org/10.1080/02670836.2016.1160195>
6. Zhang, H.; Xie, Y.; Huang, L.; Huang, S.; Zheng, X.; Chen, G.: Effect of feedstock particle sizes on wear resistance of plasma sprayed Fe-based amorphous coatings. *Surf. Coat. Technol.* **258**, 495–502 (2014). <https://doi.org/10.1016/j.surfcoat.2014.08.050>
7. Jiang, C.P.; Xing, Y.Z.; Zhang, F.Y.; Hao, J.M.: Microstructure and corrosion resistance of Fe/Mo composite amorphous coatings prepared by air plasma spraying. *Int. J. Miner. Metall. Mater.* **19**, 657–662 (2012). <https://doi.org/10.1007/s12613-012-0609-z>
8. Yin, Z.; Tao, S.; Zhou, X.; Ding, C.: Particle in-flight behavior and its influence on the microstructure and mechanical properties of plasma-sprayed Al₂O₃ coatings. *J. Eur. Ceram. Soc.* **28**, 1143–1148 (2008). <https://doi.org/10.1016/j.jeurceramsoc.2007.09.050>
9. Student, M.M.; Pokhmurs'ka, H.V.; Zadorozhna, K.R.; Veseliv's'ka, H.H.; Hvozdet's'kyi, V.M.; Sirak, Y.Y.: Corrosion resistance of VC–FeCr and VC–FeCrCo coatings obtained by supersonic gas-flame spraying. *Mater. Sci.* **54**, 535–541 (2019). <https://doi.org/10.1007/s11003-019-00214-1>
10. Farmer, J.C.; Choi, J.; Saw, C.; Haslam, J.; Day, D.; Lian, T.; Rebak, R.; Perepezko, J.; Payer, J.; Beardsley, B.; Amato, A.D.; Aprigliano, L.: Iron-based amorphous-metals: high performance corrosion-resistant material (HPCRM) Development. *Metall. Trans. A* **40A**, 1289–1305 (2009)
11. Ni, H.S.; Liu, X.H.; Chang, X.C.; Hou, W.L.; Liu, W.; Wang, J.Q.: High performance amorphous steel coating prepared by HVOF thermal spraying. *J. Alloy. Compd.* **467**, 163–167 (2009). <https://doi.org/10.1016/j.jallcom.2007.11.133>
12. Otsubo, F.; Kishitake, K.: Corrosion resistance of Fe-16%Cr-30%Mo-(C, B, P) amorphous coatings sprayed by HVOF and APS processes. *Mater. Trans.* **46**, 80–83 (2005)
13. Inoue, A.; Wang, X.M.; Zhang, W.: Developments and applications of bulk metallic glasses. *Rev. Adv. Mater. Sci.* **18**, 1–9 (2008). <https://doi.org/10.1249/01.MSS.0000149808.38194.21>
14. Chokethawai, K.; McCartney, D.G.; Shipway, P.H.: Microstructure evolution and thermal stability of an Fe-based amorphous alloy powder and thermally sprayed coatings. *J. Alloy. Compd.* **480**, 351–359 (2009). <https://doi.org/10.1016/j.jallcom.2009.02.035>
15. Zhou, Z.; Wang, L.; He, D.Y.; Wang, F.C.; Liu, Y.B.: Microstructure and electrochemical behavior of Fe-based amorphous metallic coatings fabricated by atmospheric plasma spraying. *J. Therm.*



- Spray Technol. **20**, 344–350 (2011). <https://doi.org/10.1007/s11666-010-9570-4>
16. Yang, Q.; Li, R.; Liu, Z.Q.; Shi, M.J.; Luo, X.K.; Zhang, T.: Compositional dependence of microstructure and tribological properties of plasma sprayed Fe-based metallic glass coatings. *Sci. China Technol. Sci.* **55**, 1335–1342 (2012). <https://doi.org/10.1007/s11431-012-4821-x>
 17. Guo, W.; Wu, Y.; Zhang, J.; Hong, S.; Li, G.; Ying, G.; Guo, J.; Qin, Y.: Fabrication and characterization of thermal-sprayed Fe-based amorphous / nanocrystalline composite coatings: an overview. *J. Therm. Spray Technol.* **23**, 1157–1180 (2014). <https://doi.org/10.1007/s11666-014-0096-z>
 18. Vardelle, M.; Fauchais, P.; Vardelle, A.; Li, K.I.; Dussoubs, B.; Themelis, N.J.: Controlling particle injection in plasma spraying. *J. Therm. Spray Technol.* **10**, 267–284 (2001). <https://doi.org/10.1361/105996301770349367>
 19. Aruna, S.T.; Balaji, N.; Shedthi, J.; Grips, V.K.W.: Effect of critical plasma spray parameters on the microstructure, microhardness and wear and corrosion resistance of plasma sprayed alumina coatings. *Surf. Coat. Technol.* **208**, 92–100 (2012). <https://doi.org/10.1016/j.surfcoat.2012.08.016>
 20. Zhang, C.; Guo, R.Q.; Yang, Y.; Wu, Y.; Liu, L.: Influence of the size of spraying powders on the microstructure and corrosion resistance of Fe-based amorphous coating. *Electrochim. Acta* **56**, 6380–6388 (2011). <https://doi.org/10.1016/j.electacta.2011.05.020>
 21. Zhang, C.; Chu, Z.; Wei, F.; Qin, W.; Yang, Y.; Dong, Y.; Huang, D.; Wang, L.: Optimizing process and the properties of the sprayed Fe-based metallic glassy coating by plasma spraying. *Surf. Coat. Technol.* **319**, 1–5 (2017). <https://doi.org/10.1016/j.surfcoat.2017.03.063>
 22. II Shin, D.; Gitzhofer, F.; Moreau, C.: Properties of induction plasma sprayed iron based nanostructured alloy coatings for metal based thermal barrier coatings. *J. Thermal Spray Technol.* **16**, 118–127 (2007). <https://doi.org/10.1007/s11666-006-9003-6>
 23. Li, G.; Gan, Y.; Liu, C.; Shi, Y.; Zhao, Y.; Kou, S.: Corrosion and wear resistance of Fe-based amorphous coatings. *Coatings* **10**, 73 (2020). <https://doi.org/10.3390/coatings10010073>
 24. Pukasiewicz, A.G.M.; de Boer, H.E.; Sucharski, G.B.; Vaz, R.F.; Procopiak, L.A.J.: The influence of HVOF spraying parameters on the microstructure, residual stress and cavitation resistance of FeMnCrSi coatings. *Surf. Coat. Technol.* **327**, 158–166 (2017). <https://doi.org/10.1016/J.SURFCOAT.2017.07.073>
 25. Sorour, A.A.; Adeniyi, S.A.; Hussein, M.A.; Kim, C.P.; Al-Aqeeli, N.M.: Densification And Microstructure Of Fe-Cr-Mo-B-C alloy fabricated by spark plasma sintering. In: *Materials Science and Technology 2018 (MS&T18)*, pp. 1454–1461 (2018)
 26. Schindelin, J.; Arganda-Carreras, I.; Frise, E.; Kaynig, V.; Longair, M.; Pietzsch, T.; Preibisch, S.; Rueden, C.; Saalfeld, S.; Schmid, B.; Tinevez, J.-Y.; White, D.J.; Hartenstein, V.; Eliceiri, K.; Tomancak, P.; Cardona, A.: Fiji: an open-source platform for biological-image analysis. *Nat Methods.* **9**, 676–682 (2012). <https://doi.org/10.1038/nmeth.2019>
 27. Oliver, W.C.; Pharr, G.M.: Measurement of hardness and elastic modulus by instrumented indentation: Advances in understanding and refinements to methodology. *J. Mater. Res.* **19**, 3–20 (2011). <https://doi.org/10.1557/jmr.2004.19.1.3>
 28. Pawlowski, L.: *The Science and Engineering of Thermal Spray Coatings: Second Edition.* (2008)
 29. Vardelle, A.; Vardelle, M.; Fauchais, P.; Proulx, P.; Boulos, M.I.: Loading effect by oxide powders in dc plasma jet. In: *Thermal Spray: International Advances in Coatings Technology*, C.C. Berndt (Ed.), ASM International, Materials Park, OH, pp. 543–547 (1992)
 30. Feng, Z.G.; Domaszewski, M.; Montavon, G.; Coddet, C.: Finite element analysis of effect of substrate surface roughness on liquid droplet impact and flattening process. *J. Therm. Spray Technol.* **11**, 62–68 (2002). <https://doi.org/10.1361/105996302770348989>
 31. Zhou, Z.; Wang, L.; Wang, F.C.; Zhang, H.F.; Liu, Y.B.; Xu, S.H.: Formation and corrosion behavior of Fe-based amorphous metallic coatings by HVOF thermal spraying. *Surf. Coat. Technol.* **204**, 563–570 (2009). <https://doi.org/10.1016/j.surfcoat.2009.08.025>
 32. Ha, H.M.; Payer, J.H.: Devitrification of Fe-based amorphous metal SAM 1651: a structural and compositional study. *Metall. Mater. Trans. A* **40**, 2519–2529 (2009). <https://doi.org/10.1007/s11661-009-9977-z>
 33. Cheng, J.B.; Liang, X.B.; Xu, B.S.: Devitrification of arc-sprayed FeBSiNb amorphous coatings: effects on wear resistance and mechanical behavior. *Surf. Coat. Technol.* **235**, 720–726 (2013). <https://doi.org/10.1016/j.surfcoat.2013.08.054>
 34. Souza, C.A.C.; Ribeiro, D.V.; Kiminami, C.S.: Corrosion resistance of Fe-Cr-based amorphous alloys: an overview. *J. Non-Cryst. Solids* **442**, 56–66 (2016). <https://doi.org/10.1016/j.jnoncrysol.2016.04.009>
 35. Yang, Y.; Zhang, C.; Peng, Y.; Yu, Y.; Liu, L.: Effects of crystallization on the corrosion resistance of Fe-based amorphous coatings. *Corros. Sci.* **59**, 10–19 (2012). <https://doi.org/10.1016/j.corsci.2012.02.003>
 36. Duarte, M.J.; Kostka, A.; Jimenez, J.A.; Choi, P.; Klemm, J.; Crespo, D.; Raabe, D.; Renner, F.U.: Crystallization, phase evolution and corrosion of Fe-based metallic glasses: an atomic-scale structural and chemical characterization study. *Acta Mater.* **71**, 20–30 (2014). <https://doi.org/10.1016/j.actamat.2014.02.027>
 37. Keller, L.; Dollase, W.A.: X-ray determination of crystalline hydroxyapatite to amorphous calcium- phosphate ratio in plasma sprayed coatings. *J. Biomed. Mater. Res.* **49**, 244–249 (2000). [https://doi.org/10.1002/\(SICI\)1097-4636\(200002\)49:2%3c244::AID-JBM13%3e3.0.CO;2-H](https://doi.org/10.1002/(SICI)1097-4636(200002)49:2%3c244::AID-JBM13%3e3.0.CO;2-H)
 38. Erdemir, F.: Study on particle size and X-ray peak area ratios in high energy ball milling and optimization of the milling parameters using response surface method. *Measurement* **112**, 53–60 (2017). <https://doi.org/10.1016/j.measurement.2017.08.021>
 39. Yoon, S.; Kim, J.; Bae, G.; Kim, B.; Lee, C.: Formation of coating and tribological behavior of kinetic sprayed Fe-based bulk metallic glass. *J. Alloy. Compd.* **509**, 347–353 (2011). <https://doi.org/10.1016/j.jallcom.2010.09.024>
 40. Liu, L.; Zhang, C.: Fe-based amorphous coatings: Structures and properties. *Thin Solid Films* **561**, 70–86 (2014). <https://doi.org/10.1016/j.tsf.2013.08.029>
 41. Lu, J.Z.; Cao, J.; Lu, H.F.; Zhang, L.Y.; Luo, K.Y.: Wear properties and microstructural analyses of Fe-based coatings with various WC contents on H13 die steel by laser cladding. *Surf. Coat. Technol.* **369**, 228–237 (2019). <https://doi.org/10.1016/J.SURFCOAT.2019.04.063>
 42. Fan, L.; Dong, Y.; Chen, H.; Dong, L.; Yin, Y.: Wear properties of plasma transferred arc Fe-based coatings reinforced by spherical WC particles. *J. Wuhan Univ. Technol. Mater. Sci. Ed.* **34**:433–439 (2019). doi: <https://doi.org/10.1007/s11595-019-2070-6>
 43. Kumar, A.; Bhushan, B.: Nanomechanical, nanotribological and macrotribological characterization of hard coatings and surface treatment of H-13 steel. *Tribol. Int.* **81**, 149–158 (2015). <https://doi.org/10.1016/j.triboint.2014.08.010>
 44. Yasir, M.; Zhang, C.; Wang, W.; Xu, P.; Liu, L.: Wear behaviors of Fe-based amorphous composite coatings reinforced by Al₂O₃ particles in air and in NaCl solution. *Mater. Des.* **88**, 207–213 (2015). <https://doi.org/10.1016/j.matdes.2015.08.142>
 45. Guo, R.Q.; Zhang, C.; Yang, Y.; Peng, Y.; Liu, L.: Corrosion and wear resistance of a Fe-based amorphous coating in underground environment. *Intermetallics* **30**, 94–99 (2012). <https://doi.org/10.1016/j.intermet.2012.03.026>

46. Lim, S.C.; Ashby, M.F.: Overview no 55 wear-mechanism maps. *Acta Metall.* **35**, 1–24 (1987). [https://doi.org/10.1016/0001-6160\(87\)90209-4](https://doi.org/10.1016/0001-6160(87)90209-4)
47. Adesina, A.Y.; Gasem, Z.M.; Mohammed, A.S.: Comparative investigation and characterization of the scratch and wear resistance behavior of TiN, CrN, AlTiN and AlCrN Cathodic Arc PVD coatings. *Arab. J. Sci. Eng.* (2019). <https://doi.org/10.1007/s13369-019-04038-8>
48. Öge, M.; Kucuk, Y.; Gok, M.S.; Karaoglanli, A.C.: Comparison of dry sliding wear behavior of plasma sprayed FeCr slag coating with Cr₂O₃ and Al₂O₃–13TiO₂ coatings. *Int. J. Appl. Ceram. Technol.* **16**, 2283–2298 (2019). <https://doi.org/10.1111/ijac.13273>
49. Adesina, A.Y.; Gasem, Z.M.; Madhan Kumar, A.: Corrosion resistance behavior of single-layer cathodic Arc PVD nitride-base coatings in 1M HCl and 3.5 pct NaCl solutions. *Metall. Mater. Trans. B.* **48**, 1321–1332 (2017). <https://doi.org/10.1007/s11663-016-0891-7>
50. Sá Brito, V.R.S.; Bastos, I.N.; Costa, H.R.M.: Corrosion resistance and characterization of metallic coatings deposited by thermal spray on carbon steel. *Mater. Des.* **41**, 282–288 (2012). <https://doi.org/10.1016/j.matdes.2012.05.008>

